Plasmonic Hot Electron Induced Photocurrent Response at MoS_2—Metal Junctions

Tu Hong,[†] Bhim Chamlagain,[‡] Shuren Hu,[§] Sharon M. Weiss,[†,§] Zhixian Zhou,[‡] and Ya-Qiong Xu*[,†,§]

[†]Department of Electrical Engineering and Computer Science, Vanderbilt University, Nashville, Tennessee 37212, United States, [‡]Department of Physics and Astronomy, Wayne State University, Detroit, Michigan 48201, United States, and [§]Department of Physics and Astronomy, Vanderbilt University, Nashville, Tennessee 37212, United States

ABSTRACT We investigate the wavelength- and polarization-dependence of photocurrent signals generated at few-layer MoS_2—metal junctions through spatially resolved photocurrent measurements. When incident photon energy is above the direct bandgap of few-layer MoS_2, the maximum photocurrent response occurs for the light polarization direction parallel to the metal electrode edge, which can be attributed to photovoltaic effects. In contrast, if incident photon energy is below the direct bandgap of MoS_2, the photocurrent response is maximized when the incident light is polarized in the direction perpendicular to the electrode edge, indicating different photocurrent generation mechanisms. Further studies show that this polarized photocurrent response can be interpreted in terms of the polarized absorption of light by the plasmonic metal electrode, its conversion into hot electron—hole pairs, and subsequent injection into MoS_2. These fundamental studies shed light on the knowledge of photocurrent generation mechanisms in metal—semiconductor junctions, opening the door for engineering future two-dimensional materials based optoelectronics through surface plasmon resonances.

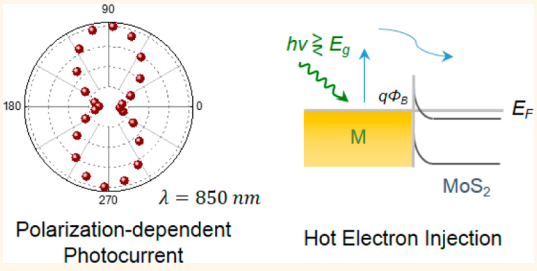

KEYWORDS: plasmonics · scanning photocurrent microscopy · MoS_2 · photovoltaic effect · photothermoelectric effect · polarization

The development of two-dimensional (2D) materials, such as graphene and transition metal dichalcogenides (TMDCs), has opened up new horizons in the realm of physics and engineering that could lead to the revolution of future nanoelectronics, optoelectronics, and energy harvesting.[1−5] One of the most promising applications of 2D materials is for photodetectors.[6−11] Various hybrid structures have been developed to enhance the photoresponse in 2D materials.[6−14] Among them the simplest configuration is the metal−2D material−metal device, in which the photocurrent can be generated at metal−2D material junctions. Metal−molybdenum disulfide (MoS_2)−metal devices have attracted much interest for photodetector applications due to their potential for achieving ultrahigh sensitivity.[6] Intensive research efforts have focused on elucidating the physical mechanisms that give rise to photoconductivity in metal−MoS_2-metal devices.[6,15−18] Two major mechanisms have been proposed to explain the photocurrent response at MoS_2—metal junctions: photovoltaic effect (PVE) and photothermoelectric effect (PTE).[6,15,16]

Recently, plasmon excitations in metallic nanostructures have been demonstrated to modulate the structural and optical properties of MoS_2 and other 2D materials. For example, hot carrier injection can change the doping of graphene[19] and induce structural phase transitions in MoS_2.[20,21] The efficiency of the hydrogen evolution reaction can also be enhanced by depositing Au-coated Ag nanorattles on MoS_2 to induce its localized phase transition under plasmon resonance excitation.[22] Moreover, the photoluminescence of MoS_2 can be influenced by surface plasmons of Au nanoantennas, where the photoluminescence intensity is significantly enhanced and strongly dependent on the incident polarization when the wavelength is close to resonance with the surface plasmons of nanoantennas.[23] The surface plasmon resonances induced by metals may also affect the photocurrent response at MoS_2—metal

* Address correspondence to yaqiong.xu@vanderbilt.edu.

Received for review February 14, 2015 and accepted April 14, 2015.

Published online April 14, 2015
10.1021/acsnano.5b01065

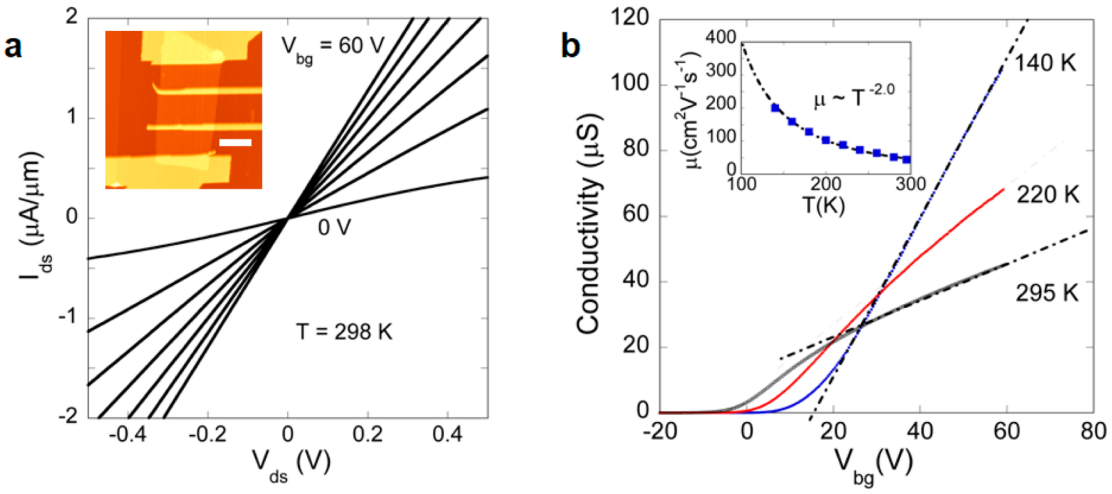

Figure 1. Electrical transport characterization of a 9 nm thick MoS_2 FET. (a) Output characteristics of the device measured at various gate voltages between 0 and 60 V. Inset: AFM image of the device. The scale bar is 2 μm. (b) Four-terminal conductivity of the device measured with the back-gate voltage sweeping from −20 to 60 V at different temperatures. Inset: Field-effect mobility as a function of temperature estimated from the four-terminal conductivity in the gate voltage ranging from 40 to 60 V.

junctions. It is, therefore, desirable to study the relative contributions of PVE, PTE, and surface plasmons to the overall photoresponse at MoS_2−metal junctions. Understanding the photon−electron conversion mechanisms at MoS_2−metals will offer a new approach for engineering future 2D material based optoelectronics.

Here, we investigate the polarization- and wavelength-dependence of photocurrent signals generated at few-layer MoS_2−metal junctions through spatially resolved photocurrent measurements. When incident photon energy is above the direct bandgap of few-layer MoS_2, the maximum photocurrent response occurs for the light polarization direction parallel to the metal electrode edge. This anisotropic photocurrent response may result from the light-generated anisotropic distribution of carriers in momentum space, which has been demonstrated in the photoresponse at graphene−metal junctions.[24] Interestingly, we find that if incident photon energy is below the direct bandgap of MoS_2, the photocurrent intensity is reduced by 2 orders of magnitude and mainly attributed to the polarized absorption of the plasmonic Au electrodes. When the wavelength is close to resonance with the surface plasmons of the Au electrodes, the photocurrent intensity is strongly dependent on the incident polarization with about 8 times larger for laser polarization perpendicular to the metal electrode than for parallel polarization. Plasmonically engineered photocurrent response in metal−semiconductor junctions may provide a new way to design future 2D photodetectors, in particular, in the near-infrared and infrared regimes.

RESULTS AND DISCUSSION

Few-layer MoS_2 crystals (6 nm −10 nm) were produced by repeated splitting of bulk crystals using a mechanical cleavage method, and subsequently transferred to a degenerately doped Si substrate with 290 nm SiO_2. To minimize charged impurities and charge traps on the substrate surface, the Si/SiO_2 substrates were covered with crystalline self-assembled monolayers (SAMs) of octadecyltrimethoxysilane (OTMS) prior to the transfer of mechanically exfoliated MoS_2 flakes.[25,26] Optical microscopy was used to identify thin MoS_2 crystals, which were further characterized by Park-Systems XE-70 noncontact atomic force microscopy (AFM). MoS_2 field effect transistors (FETs) were subsequently fabricated using standard electron beam lithography and electron beam deposition of 5 nm Ti and 40 nm Au, where the Si substrate is used as the back gate. An AFM image of a typical MoS_2 device is shown in the inset of Figure 1a, where the length of metal electrodes is 10 μm and the widths of the wide and narrow electrodes are 2 μm and 200 nm, respectively. Electrical properties of the devices were measured by a Keithley 4200 semiconductor parameter analyzer in a Lakeshore cryogenic probe station under high vacuum (1×10^{-6} Torr). Figure 1 shows the electrical characteristics of a 9 nm thick MoS_2 FET (as determined by AFM). The $I_{ds}-V_{ds}$ curves exhibit ohmic characteristic for gate voltages steping from 0 to 60 V, indicating a negligible Schottky barrier between the Au electrodes and MoS_2 (Figure 1a), in agreement with a previous report (~50 meV).[27] The device displays a predominately n-type behavior, with the estimated room-temperature field-effect mobility $\mu \sim 50\ cm^2\ V^{-1}\ s^{-1}$ as extracted from the gate dependence of four-terminal conductivity σ (Figure 1b).[28] As the temperature decreases, the mobility increases following a $\mu \sim T^{-2.0}$ dependence, consistent with the recent results on high quality MoS_2 encapsulated by boron nitride (Figure 1b inset).[29]

To investigate the local photoresponse at MoS_2−metal junctions, we performed spatially resolved scanning

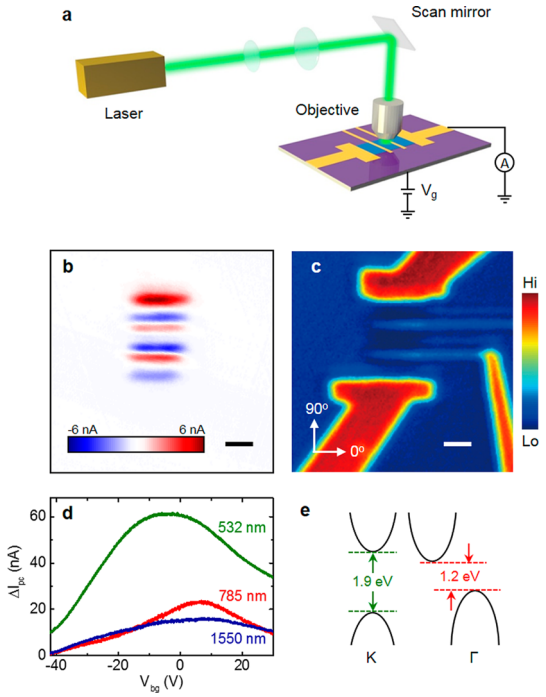

Figure 2. (a) Schematic illustration of the MoS_2 device and the optical setup. (b) Scanning photocurrent image and (c) reflection image of the MoS_2 device illuminated by 785 nm laser. Incident light polarization directions are defined as marked, where 0° denotes polarization direction along the metal electrode edge and 90° denotes polarization direction perpendicular to the metal electrode edge. The scale bars are 2 μm. (d) Photocurrent response of the MoS_2 FET as a function of gate voltage with illumination of 532 nm (green curve), 785 nm (red curve), and 1550 nm (blue curve) laser, respectively. The source-drain bias is 10 mV. The lasers were defocused to form a spot large enough to cover the entire MoS_2 flake. (e) Band structure of few-layer MoS_2, an indirect bandgap semiconductor with a direct bandgap at K (−K) points. The valence band splitting is not shown.

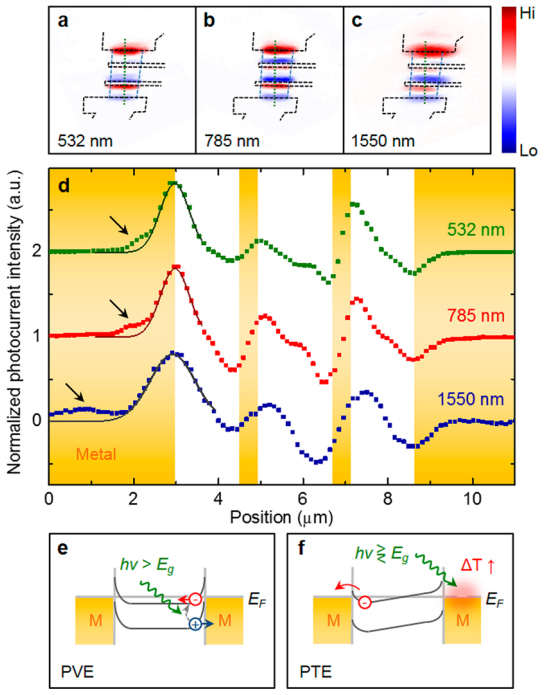

Figure 3. Scanning photocurrent images of MoS_2 illuminated by (a) 532 nm, (b) 785 nm, and (c) 1550 nm laser, respectively. The black dashed lines outline the metal electrodes, whereas the blue dashed lines mark the MoS_2 edges. The intensities of the photocurrent response are normalized. (d) Line profiles of the photocurrent response along the dashed green lines in (a−c). The photocurrent intensities are displaced for clarity. The solid curves are Gaussian fits of the line profiles at the MoS_2-metal junction. The black arrows denote the photocurrent "tails" on the electrodes. The orange background indicates electrode positions. (e) Schematic illustration of PVE and (f) PTE mechanisms. E_g represents the bandgap of MoS_2.

photocurrent measurements in an Olympus microscope setup (Figure 2a). A linearly polarized continuous wave laser source was expanded and altered by a nanometer-resolution scan mirror. The laser beam was then focused by a 40× objective (N.A. = 0.6) into a diffraction-limited spot (~1 μm) on the samples. The polarization direction of the laser beam was changed by a half-wave plate followed by a polarizer. All experiments were performed in high vacuum (1×10^{-6} Torr). Figure 2b shows a scanning photocurrent image of a MoS_2 device at zero bias, whose corresponding reflection image was recorded simultaneously (Figure 2c). The outer two electrodes of the MoS_2 FET were used as source and drain while the middle two electrodes were floating during the measurement. Figure 2d shows the photocurrent signals $\Delta I_{pc} = I_{ds,illumination} - I_{ds,dark}$ under laser illumination of three different wavelengths (532, 785, and 1550 nm), where the source-drain bias is 10 mV. With 532 nm (2.33 eV) illumination, a significant photocurrent response is mainly attributed to the increment of electrons that are efficiently excited through a direct bandgap close to 1.9 eV at K(-K) points (Figure 2e).[30,31] As a result, the direct bandgap transition and PTE will be responsible for the photocurrent response. The photocurrent signals induced by 785 nm (1.58 eV) excitation may be related to the indirect bandgap optical transition between Brillouin zone Γ point and K point in few-layer MoS_2 (1.2 eV). This process requires a phonon to change the momentum, resulting in a relatively low quantum efficiency and leading to a significant reduction of PVE-induced photocurrent response. Moreover, there is a non-negligible photocurrent response upon 1550 nm (0.8 eV) illumination, whose photon energy is not enough to excite electrons from the valence band of MoS_2. Here, the PVE induced by the indirect bandgap transition does not contribute to the photocurrent response. Therefore, PTE or other new mechanisms are required to explain the photocurrent generation when the photon energy is below the direct bandgap of MoS_2.

To clarify the photocurrent generation mechanisms in MoS_2−metal junctions, we look into the spatially resolved scanning photocurrent images of the MoS_2 FET illuminated by 532, 785, and 1550 nm laser, respectively (Figure 3a−c). The black dashed lines are

the edges of the metal electrodes, and the blue dashed lines show the edges of the MoS_2. A line profile of photocurrent intensities in each image is extracted along the dashed green line in the vertical direction and presented in Figure 3d. The photocurrent intensities were normalized and displaced for clarity, and the solid curves are Gaussian fittings of the photocurrent values. The strongest photocurrent responses are observed at the MoS_2−metal junction for illumination with different photon energies. As shown in Figure 3e, potential barriers are formed at MoS_2−metal junctions due to Fermi level alignment, leading to a built-in electric field that separates the photoexcited charge carriers when photon energies are greater than the bandgap of MoS_2 (PVE). However, when the photon energy is below the bandgap, the PVE induced photocurrent response is significantly reduced, owing to the absence of interband transitions. Moreover, by comparing the photocurrent profiles and the Gaussian fittings, we notice strong photocurrent "tails" in the metal region for all laser wavelengths as pointed by the black arrows in Figure 3d, indicating that PTE (Figure 3f) also contributes to the photocurrent generation at MoS_2−metal junctions. A temperature difference (ΔT) arises upon laser absorption due to the difference in Seebeck coefficients (S) between MoS_2 and metal electrodes. This temperature gradient leads to a photothermal voltage (V_{PTE}) across the junction,

$$V_{PTE} = (S_{MoS_2} - S_{Metal})\Delta T \quad (1)$$

From the Mott relation,[16,32] we can obtain the Seebeck coefficient as

$$S = -\frac{\pi^2 k_b^2 T}{3e}\frac{1}{G}\frac{dG}{dE}\bigg|_{E=E_F} \quad (2)$$

where k_b is the Boltzmann constant, e is the electron charge, G is conductance, and E_F is Fermi energy. We estimated the Seebeck coefficient of our MoS_2 device at different Fermi levels from eq 2 and obtained $S \sim 40$ μV/K at $V_g = 0$ V. This value increases to its maximum ($\sim 2 \times 10^3$ μV/K) when V_g approaches toward −40 V, which is comparable to the reported bulk value of MoS_2[33] and about one to 2 orders of magnitude smaller than that observed in monolayer MoS_2.[17]

To further explore the relative contributions of different photocurrent generation mechanisms to the overall photocurrent response, we performed polarization-dependent photocurrent measurements, where 0° denotes the polarization direction along the metal-MoS_2 contact edge (Figure 2c). The photocurrent response at a MoS_2-metal junction was systematically investigated when the junction was illuminated by lasers from 500 nm (2.48 eV) to 1050 nm (1.18 eV) in 50 nm steps. As shown in Figure 4, the maximum photocurrent response occurs at 90° light polarization for lasers with photon energies below the direct bandgap of MoS_2 (with wavelength of 750 nm or longer), whereas the maximum photocurrent is generated by photons polarized at around 0° when the excitation photon energy is above the direct bandgap of MoS_2 (with laser wavelength of 650 nm or shorter). Since PTE should be isotropic and independent of the incoming light polarization, the generation of thermally induced charge carriers could not explain our observation. If the photon energy is high enough to excite carriers through the direct bandgap at K (−K) points in MoS_2 Brillouin zone, the built-in electric field at MoS_2−metal junctions can separate the photoexcited charge carriers to generate photocurrent (PVE). The polarization dependence measurements suggest that the interband transition at K (-K) points is maximized when photons are polarized parallel to the electrode edges. This result indicates that the valence electrons in MoS_2 prefer to absorb photons with the polarization direction perpendicular to the momentum of electrons. A similar phenomenon has been demonstrated in the photoresponse at graphene-metal junctions, in which it was shown that when the polarization angle of the incident light is perpendicular to the momentum of electrons, the absorption of light for valence electrons in graphene is maximum, leading to anisotropic photocurrent signals.[24]

When the excitation laser energy is below the direct bandgap (1.9 eV) of MoS_2 (especially below the indirect bandgap of 1.2 eV), a new mechanism is needed to explain the photocurrent generation due to the absence of optical transitions through the bandgap. It is well-known that photoexcited hot electrons in metal electrodes can cross over the Schottky barrier and be injected into the conduction band of semiconductors (Figure 5a). The Schottky barrier between Au electrodes and few-layer MoS_2 is very small as demonstrated in our electrical transport measurements (Figure 1a) and previous studies (~50 meV),[27] which is well below the excitation photon energies in our experiments. The injection yield of hot electrons Y follows the Fowler equation

$$Y \sim \frac{1}{8E_F}\frac{(\hbar\omega - \phi_B)^2}{\hbar\omega} \quad (3)$$

where $\hbar$ is the reduced plank constant, ω is the incident light frequency, ϕ_B is the Schottky barrier, and E_F is Fermi energy. The injection yield depends on the wavelength of the excitation light instead of its polarization, which cannot explain the polarization dependence of photocurrent signals. In fact, the photocurrent response depends on not only the injection yield of hot electrons but also the metal absorption. As shown in Figure 5b, when the illumination wavelength is close to 850 nm, the anisotropic ratio of the photocurrent response ($I_{pc}^{90°}/I_{pc}^{0°}$) achieves its maximum (~8), which is significantly reduced when the width of the

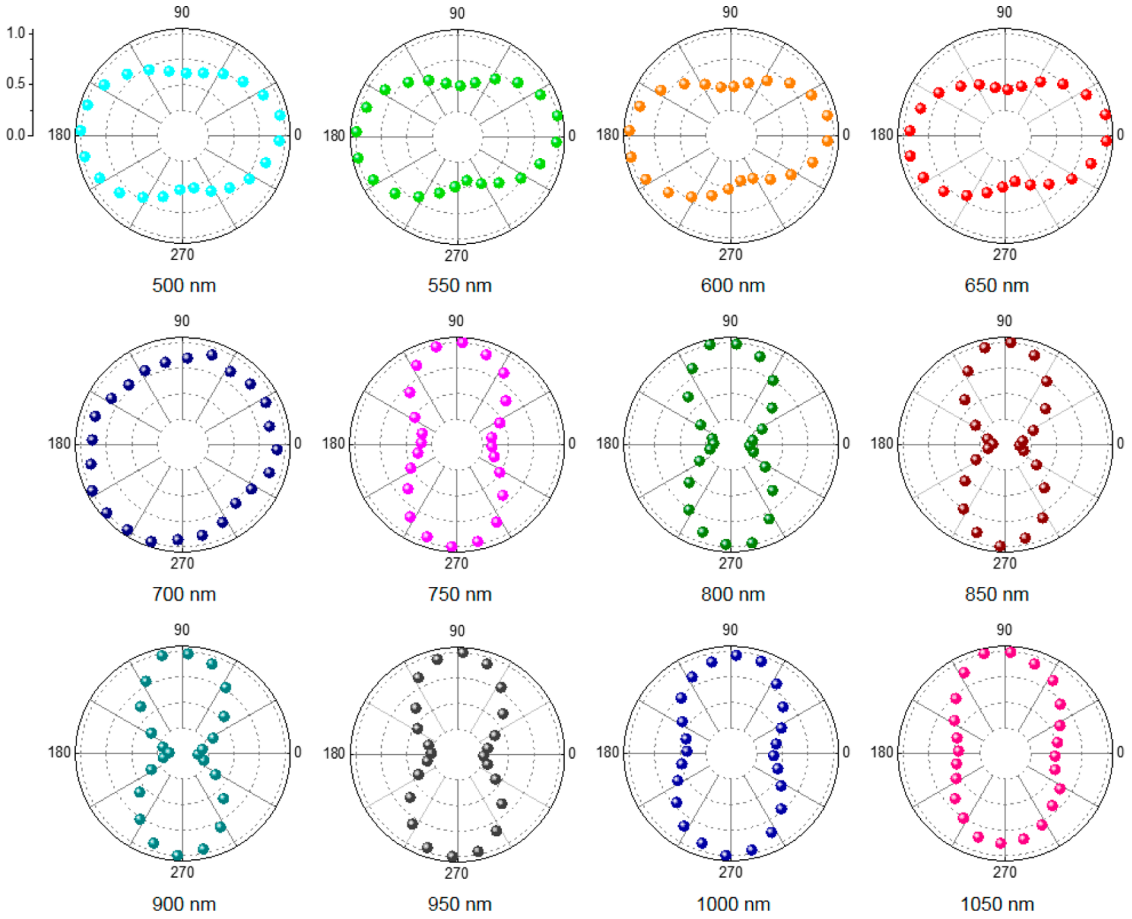

Figure 4. Normalized photocurrent intensities at a MoS_2-metal junction (200 nm-wide metal electrode) as a function of incident light polarization with illumination wavelength from 500 to 1050 nm. Gate voltage and source-drain bias were 0 V during the measurements.

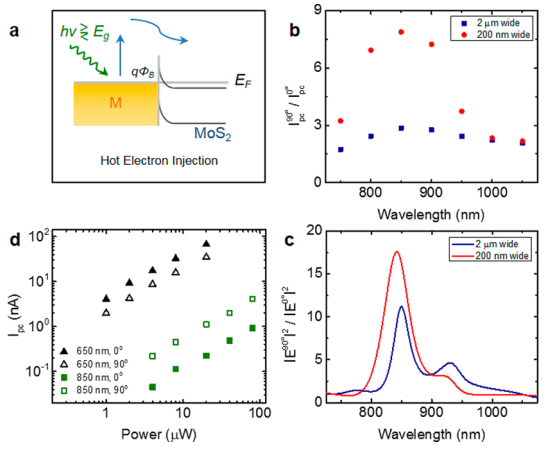

Figure 5. (a) Schematic illustration of hot electron injection from a metal electrode to MoS_2. E_g represents the bandgap of MoS_2. (b) The wavelength dependence of measured photocurrent response ($I_{pc}^{90°}/I_{pc}^{0°}$) at MoS_2-metal junctions. (c) The calculated $|E^{90°}|^2/|E^{0°}|^2$ of metal electrodes by using FDTD as a function of wavelength. (d) Photocurrent power dependence with 650 nm (1.91 eV, black triangles) and 850 nm (1.46 eV, green squares) laser polarized in 0° (solid) and 90° (hollow).

metal electrode increase from 200 nm to 2 μm. The metal absorption I_{ab} is proportional to the energy flux, which is related to its respective electric field through the time-averaged Poynting vector S:

$$I_{pc} \sim I_{ab} \sim \langle S \rangle_{time} \sim |E|^2 \quad (4)$$

The $|E|^2$ ratio between two polarizations is calculated using finite difference time domain (FDTD) simulations (Figure 5c). The geometries are chosen according to device dimensions measured by AFM. The calculated $|E^{90°}|^2/|E^{0°}|^2$ shows a resonance peak at 850 nm, in good agreement with the resonance peak observed in photocurrent measurements. Moreover, the resonance intensity of $|E^{90°}|^2/|E^{0°}|^2$ is reduced by increasing the width of electrode from 200 nm to 2 μm. The relatively low anisotropic ratio of photocurrent in our devices may result from shape imperfections and the strong absorption of the Ti adhesion layer in the near-infrared regions, which can lead to a strong damping of the surface plasmon resonance.[34,35] The consistence of the resonance between the calculated $|E^{90°}|^2/|E^{0°}|^2$ of metal electrodes and photocurrent measurements ($I_{pc}^{90°}/I_{pc}^{0°}$) confirms that the polarized photocurrent response can be primarily attributed to the surface plasmon resonance in metal electrodes. We also performed power dependence measurements of the photocurrent

response at a MoS_2-metal junction. Both PVE (650 nm) and surface plasmon (850 nm) induced photocurrent signals have a linear dependence with incident power (Figure 5d), while the PVE induced photocurrent response is 2 orders of magnitude greater than photocurrent signals generated through surface plasmons in metal electrodes.

CONCLUSIONS

In conclusion, we investigate the relative contributions of PVE, PTE, and surface plasmons to the overall photoresponse at MoS_2-metal junctions through polarization- and wavelength-dependent scanning photocurrent measurements. We demonstrate that when incident photon energy is above the direct bandgap of few-layer MoS_2, the photocurrent response is primarily attributed to PVE and maximized for the light polarization direction parallel to the metal electrode edge. When the incident photon energy is below the direct bandgap of MoS_2, the photocurrent signals mainly result from surface plasmons of Au electrodes, which are 2 orders of magnitude smaller than those induced by PVE. These fundamental studies may offer a new design rule for future 2D material based photodetectors, in particular, in the near-infrared and infrared regimes.

METHODS

Device Fabrication and Electrical Characterization. Degenerately p-doped silicon substrate with 290 nm of thermally grown SiO_2 was first treated by oxygen plasma for 10 min to enhance hydrophilicity. Subsequently, a 3 mM octadecyltrimethoxysilane (OTMS) (from Sigma− Aldrich) solution in trichloroethylene was drop-casted on the substrate and allowed to assemble for 10 s. The substrate was then spun at 3000 rpm for 10 s to uniformly cover the entire surface followed by immersion in ammonia (NH_3) vapor at room temperature overnight. Finally, the substrate was rinsed with deionized (DI) water and bath sonicated in toluene for about 5 min. Multilayer MoS_2 flakes were produced by mechanical exfoliation of MoS_2 crystals (from SPI) and subsequently transferred to the OTMS-SAM-modified SiO_2 substrates. Optical microscopy and Park-Systems XE-70 noncontact mode atomic microscopy (AFM) were used to identify and characterize thin MoS_2 flakes. Four-probe MoS_2 FET devices were fabricated using standard electron beam lithography and subsequent electron beam deposition of 5 nm of Ti covered by 40 nm of Au. Electrical properties of the devices were measured by a Keithley 4200 semiconductor parameter analyzer in a lakeshore Cryogenic probe station under high vacuum (1×10^{-6} Torr).

Scanning Photocurrent Measurements. Spatially resolved scanning photocurrent measurements were performed in an Olympus microscope setup. A linearly polarized continuous wave laser source was expanded and its position was changed by a nanometer-resolution scan mirror. A 40× objective (N.A. = 0.6) was used to focus the laser beam into a diffraction-limited spot (~1 μm) on the samples. The polarization direction of the laser beam was changed by a half-wave plate followed by a polarizer. All experiments were performed in high vacuum (1×10^{-6} Torr).

FDTD Simulations. The $|E|^2$ ratio was calculated using three-dimensional finite-difference time-domain simulations (Lumerical FDTD Solutions) with the following specifications. The geometries were chosen to match the device dimensions. The light source was defined as a plane wave. The mesh size was a uniform 4 nm and the entire simulation space was surrounded by a perfectly matched layer (PML) that absorbed any fields reaching the boundaries. Frequency domain field and power monitors were used to record the optical field at the interface between electrodes and the underlying SiO_2. The width of the optical field monitors was set to be 2 μm wider than the electrodes such that the optical field within 1 μm from the edges of electrodes would be collected.

Conflict of Interest: The authors declare no competing financial interest.

Acknowledgment. This work was supported by the National Science Foundation (ECCS-1055852 and CBET-1264982 to Y.X.; ECCS-1128297 and DMR-1308436 to Z.Z.; ECCS-1407777 to S.W.).

REFERENCES AND NOTES

1. Bonaccorso, F.; Sun, Z.; Hasan, T.; Ferrari, A. C. Graphene Photonics and Optoelectronics. *Nat. Photonics* **2010**, *4*, 611–622.
2. Wang, Q. H.; Kalantar-Zadeh, K.; Kis, A.; Coleman, J. N.; Strano, M. S. Electronics and Optoelectronics of Two-Dimensional Transition Metal Dichalcogenides. *Nat. Nanotechnol.* **2012**, *7*, 699–712.
3. Xu, M. S.; Liang, T.; Shi, M. M.; Chen, H. Z. Graphene-Like Two-Dimensional Materials. *Chem. Rev.* **2013**, *113*, 3766–3798.
4. Novoselov, K. S.; Fal'ko, V. I.; Colombo, L.; Gellert, P. R.; Schwab, M. G.; Kim, K. A Roadmap for Graphene. *Nature* **2012**, *490*, 192–200.
5. Jariwala, D.; Sangwan, V. K.; Lauhon, L. J.; Marks, T. J.; Hersam, M. C. Emerging Device Applications for Semiconducting Two-Dimensional Transition Metal Dichalcogenides. *ACS Nano* **2014**, *8*, 1102–1120.
6. Lopez-Sanchez, O.; Lembke, D.; Kayci, M.; Radenovic, A.; Kis, A. Ultrasensitive Photodetectors Based on Monolayer MoS_2. *Nat. Nanotechnol.* **2013**, *8*, 497–501.
7. Britnell, L.; Ribeiro, R. M.; Eckmann, A.; Jalil, R.; Belle, B. D.; Mishchenko, A.; Kim, Y. J.; Gorbachev, R. V.; Georgiou, T.; Morozov, S. V.; et al. Strong Light-Matter Interactions in Heterostructures of Atomically Thin Films. *Science* **2013**, *340*, 1311–1314.
8. Yu, W. J.; Liu, Y.; Zhou, H. L.; Yin, A. X.; Li, Z.; Huang, Y.; Duan, X. F. Highly Efficient Gate-Tunable Photocurrent Generation in Vertical Heterostructures of Layered Materials. *Nat. Nanotechnol.* **2013**, *8*, 952–958.
9. Koppens, F. H. L.; Mueller, T.; Avouris, P.; Ferrari, A. C.; Vitiello, M. S.; Polini, M. Photodetectors Based on Graphene, Other Two-Dimensional Materials and Hybrid Systems. *Nat. Nanotechnol.* **2014**, *9*, 780–793.
10. Pospischil, A.; Furchi, M. M.; Mueller, T. Solar-Energy Conversion and Light Emission in an Atomic Monolayer p-n Diode. *Nat. Nanotechnol.* **2014**, *9*, 257–261.
11. Baugher, B. W. H.; Churchill, H. O. H.; Yang, Y. F.; Jarillo-Herrero, P. Optoelectronic Devices Based on Electrically Tunable p-n Diodes in a Monolayer Dichalcogenide. *Nat. Nanotechnol.* **2014**, *9*, 262–267.
12. Mueller, T.; Xia, F. N. A.; Avouris, P. Graphene Photodetectors for High-Speed Optical Communications. *Nat. Photonics* **2010**, *4*, 297–301.
13. Hong, T.; Chamlagain, B.; Lin, W.; Chuang, H.-J.; Pan, M.; Zhou, Z.; Xu, Y.-Q. Polarized Photocurrent Response in Black Phosphorus Field-Effect Transistors. *Nanoscale* **2014**, *6*, 8978–8983.
14. Geim, A. K.; Grigorieva, I. V. Van der Waals Heterostructures. *Nature* **2013**, *499*, 419–425.
15. Wu, C.-C.; Jariwala, D.; Sangwan, V. K.; Marks, T. J.; Hersam, M. C.; Lauhon, L. J. Elucidating the Photoresponse of Ultrathin MoS_2 Field-Effect Transistors by Scanning

Photocurrent Microscopy. *J. Phys. Chem. Lett.* **2013**, *4*, 2508–2513.
16. Buscema, M.; Barkelid, M.; Zwiller, V.; van der Zant, H. S. J.; Steele, G. A.; Castellanos-Gomez, A. Large and Tunable Photothermoelectric Effect in Single-Layer MoS_2. *Nano Lett.* **2013**, *13*, 358–363.
17. Kwak, J. Y.; Hwang, J.; Calderon, B.; Alsalman, H.; Munoz, N.; Schutter, B.; Spencer, M. G. Electrical Characteristics of Multilayer MoS_2 FET's with MoS_2/Graphene Heterojunction Contacts. *Nano Lett.* **2014**, *14*, 4511–4516.
18. Furchi, M. M.; Polyushkin, D. K.; Pospischil, A.; Mueller, T. Mechanisms of Photoconductivity in Atomically Thin MoS_2. *Nano Lett.* **2014**, *14*, 6165–6170.
19. Fang, Z. Y.; Wang, Y. M.; Liu, Z.; Schlather, A.; Ajayan, P. M.; Koppens, F. H. L.; Nordlander, P.; Halas, N. J. Plasmon-Induced Doping of Graphene. *ACS Nano* **2012**, *6*, 10222–10228.
20. Kang, Y. M.; Najmaei, S.; Liu, Z.; Bao, Y. J.; Wang, Y. M.; Zhu, X.; Halas, N. J.; Nordlander, P.; Ajayan, P. M.; Lou, J.; et al. Plasmonic Hot Electron Induced Structural Phase Transition in a MoS_2 Monolayer. *Adv. Mater.* **2014**, *26*, 6467–6471.
21. Brongersma, M. L.; Halas, N. J.; Nordlander, P. Plasmon-Induced Hot Carrier Science and Technology. *Nat. Nanotechnol.* **2015**, *10*, 25–34.
22. Kang, Y.; Gong, Y.; Hu, Z.; Li, Z.; Qiu, Z.; Zhu, X.; Ajayan, P. M.; Fang, Z. Plasmonic Hot Electron Enhanced MoS_2 Photocatalysis in Hydrogen Evolution. *Nanoscale* **2015**, *7*, 4482–4488.
23. Najmaei, S.; Mlayah, A.; Arbouet, A.; Girard, C.; Leotin, J.; Lou, J. Plasmonic Pumping of Excitonic Photoluminescence in Hybrid MoS_2-Au Nanostructures. *ACS Nano* **2014**, *8*, 12682–12689.
24. Kim, M.; Yoon, H. A.; Woo, S.; Yoon, D.; Lee, S. W.; Cheong, H. Polarization Dependence of Photocurrent in a Metal-Graphene-Metal device. *Appl. Phys. Lett.* **2012**, *101*, 073103.
25. Ito, Y.; Virkar, A. A.; Mannsfeld, S.; Oh, J. H.; Toney, M.; Locklin, J.; Bao, Z. Crystalline Ultrasmooth Self-Assembled Monolayers of Alkylsilanes for Organic Field-Effect Transistors. *J. Am. Chem. Soc.* **2009**, *131*, 9396–9404.
26. Wang, X.; Xu, J.-B.; Wang, C.; Du, J.; Xie, W. High-Performance Graphene Devices on SiO_2/Si Substrate Modified by Highly Ordered Self-Assembled Monolayers. *Adv. Mater.* **2011**, *23*, 2464–2468.
27. Das, S.; Chen, H. Y.; Penumatcha, A. V.; Appenzeller, J. High Performance Multilayer MoS_2 Transistors with Scandium Contacts. *Nano Lett.* **2013**, *13*, 100–105.
28. Chamlagain, B.; Li, Q.; Ghimire, N. J.; Chuang, H.-J.; Perera, M. M.; Tu, H.; Xu, Y.; Pan, M.; Xaio, D.; Yan, J.; et al. Mobility Improvement and Temperature Dependence in $MoSe_2$ Field-Effect Transistors on Parylene-C Substrate. *ACS Nano* **2014**, *8*, 5079–5088.
29. Cui, X.; Lee, G.-H.; Kim, Y. D.; Arefe, G.; Huang, P. Y.; Lee, C.-H.; Chenet, D. A.; Zhang, X.; Wang, L.; Ye, F.; et al. Multi-Terminal Electrical Transport Measurements of Molybdenum Disulphide Using van der Waals Heterostructure Device Platform. **2014**, arXiv:1412.5977.
30. Mak, K. F.; Lee, C.; Hone, J.; Shan, J.; Heinz, T. F. Atomically Thin MoS_2: A New Direct-Gap Semiconductor. *Phys. Rev. Lett.* **2010**, *105*, 136805.
31. Splendiani, A.; Sun, L.; Zhang, Y. B.; Li, T. S.; Kim, J.; Chim, C. Y.; Galli, G.; Wang, F. Emerging Photoluminescence in Monolayer MoS_2. *Nano Lett.* **2010**, *10*, 1271–1275.
32. Xu, X. D.; Gabor, N. M.; Alden, J. S.; van der Zande, A. M.; McEuen, P. L. Photo-Thermoelectric Effect at a Graphene Interface Junction. *Nano Lett.* **2010**, *10*, 562–566.
33. Mansfield, R.; Salam, S. A. Electrical Properties of Molybdenite. *Proc. Phys. Soc., Sect. B* **1953**, *66*, 377.
34. Jeppesen, C.; Mortensen, N. A.; Kristensen, A. The Effect of Ti and ITO Adhesion Layers on Gold Split-Ring Resonators. *Appl. Phys. Lett.* **2010**, *97*, 263103.
35. Habteyes, T. G.; Dhuey, S.; Wood, E.; Gargas, D.; Cabrini, S.; Schuck, P. J.; Alivisatos, A. P.; Leone, S. R. Metallic Adhesion Layer Induced Plasmon Damping and Molecular Linker as a Nondamping Alternative. *ACS Nano* **2012**, *6*, 5702–5709.